

SCIENTIFIC REPORTS



OPEN

Determination of a potential quantitative measure of the state of the lung using lung ultrasound spectroscopy

Libertario Demi¹, Wim van Hove², Ruud J. G. van Sloun³, Gino Soldati⁴ & Marcello Demi⁵

B-lines are ultrasound-imaging artifacts, which correlate with several lung-pathologies. However, their understanding and characterization is still largely incomplete. To further study B-lines, lung-phantoms were developed by trapping a layer of microbubbles in tissue-mimicking gel. To simulate the alveolar size reduction typical of various pathologies, 170 and 80 μm bubbles were used for phantom-type 1 and 2, respectively. A normal alveolar diameter is approximately 280 μm . A LA332 linear-array connected to the ULA-OP platform was used for imaging. Standard ultrasound (US) imaging at 4.5 MHz was performed. Subsequently, a multi-frequency approach was used where images were sequentially generated using orthogonal sub-bands centered at different frequencies (3, 4, 5, and 6 MHz). Results show that B-lines appear predominantly with phantom-type 2. Moreover, the multi-frequency approach revealed that the B-lines originate from a specific portion of the US spectrum. These results can give rise to significant clinical applications since, if further confirmed by extensive *in-vivo* studies, the native frequency of B-lines could provide a quantitative-measure of the state of the lung.

Lung ultrasonography (LUS) was initially thought to be of marginal use because the high mismatch in acoustic impedance between air and soft-tissue causes the lungs to exhibit a very low permeability to ultrasound.

To the contrary, LUS is nowadays a fast-growing field of study since many clinicians acknowledge this diagnostic technique as a powerful, cost-effective, radiation free, and ready available alternative to standard X-ray imaging¹. However, despite extensive acoustic characterization studies²⁻⁷ and well documented medical evidence⁸⁻¹⁸, a lot is still unknown about the way US interact with lung tissue.

In fact, LUS still relies on the analysis of imaging artifacts, thus resulting in qualitative and subjective diagnosis, and lacks a dedicated imaging method developed around the acoustical properties of the lungs⁸.

One of the most discussed, and yet not fully understood, lung artifact is the so-called B-line artifact. B-lines (also known as comet tail artifacts) are defined as discrete laser-like vertical hyperechoic reverberation artifacts that arise from the pleural line, extend to the bottom of the screen without fading, and move synchronously with lung sliding. Interestingly, a correlation exists between these artifacts and the increase in extravascular lung water^{9,10}, interstitial lung diseases (ILDs)^{11,12}, non-cardiogenic lung edema¹³, interstitial pneumonia¹⁴ and lung contusion¹⁵.

In this study, in an attempt to better understand the genesis and characteristics of B-lines, we recreated these artifacts in lung-mimicking phantoms. Two different types of phantom were developed, by using two different mono-disperse micro-bubble populations. Microbubbles with a size equal to 170 and 80 μm were used for phantom-type 1 and 2, respectively. This allowed for the analysis of B-lines in a controlled environment where the alveolar size reduction, which is typical of various lung pathologies, was mimicked. Additionally, US images were generated by using an open research platform, thus providing access to the raw data and allowing for the full control of the transmission/reception parameters. These aspects are crucial, since analyzing signals after black/box signal-processing operations would have severely limited the analysis. First, standard B-mode imaging data were acquired, so as to confirm the appearance of B-lines. Subsequently, consecutive narrow-band pulses centered at different frequencies were used for imaging in order to span a large frequency range without employing a single broad-band pulse. This

¹TMC Science and Technology, Brussels, Belgium. ²Tide Microfluidics, Enschede, The Netherlands. ³Eindhoven University of Technology, Eindhoven, The Netherlands. ⁴Emergency Medicine Unit, Valle del Serchio General Hospital, Lucca, Italy. ⁵Medical Image Processing, Fondazione Toscana Gabriele Monasterio, Pisa, Italy. Correspondence and requests for materials should be addressed to L.D. (email: libertario.demi@tmceurope.com)

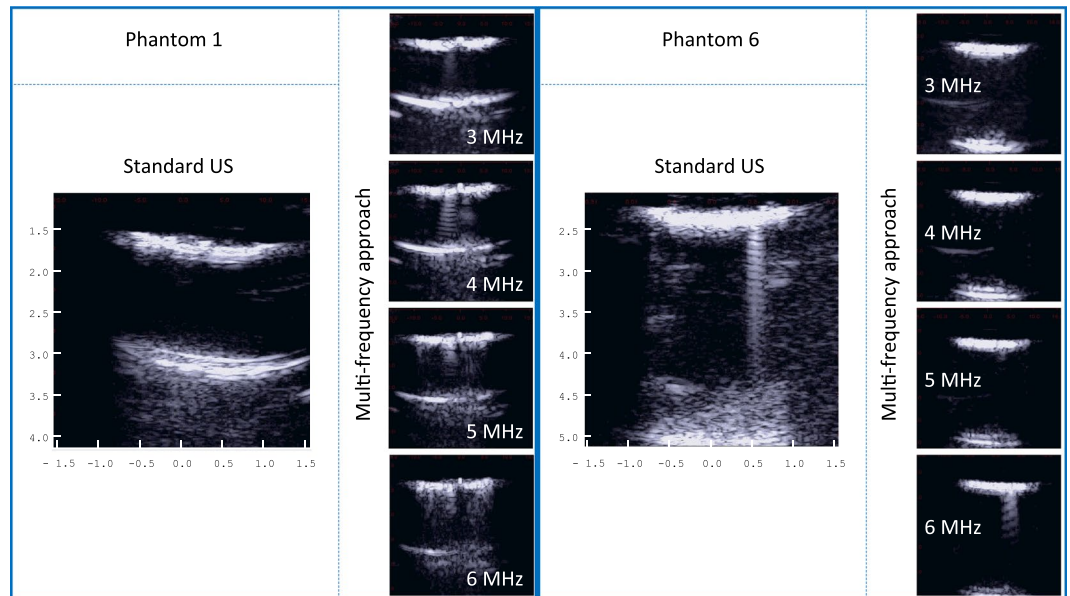


Figure 1. Example of standard US images and multi-frequency US images as obtained from phantom 1 and 6, respectively.

procedure allowed us to investigate the appearance of B-lines as a function of the emitted frequency. In fact, one of the most plausible hypotheses regarding the generation of these artifacts describes B-lines as originating from reverberations between the interstitial spaces, which are enlarged in the presence of specific lung pathologies^{8,16}. This will have the effect to locally reduce the acoustic-impedance mismatch with the intercostal tissue and, consequently, to open channels that are accessible to ultrasound. It is thus reasonable to expect the artifact to manifest itself at a specific frequency, which would then correlate to the size and shape of the interstitial space. In such a situation, the native frequency of the B-lines could thus offer a possibility to quantitatively evaluate the state of the lung surface.

Results

Visual inspection. Figure 1 shows an example of standard US images and multi-frequency US images as obtained from phantom number 1 and 6, respectively. As can be seen from the standard US images, a B-line was visible only on phantom 6, which was developed with the smaller microbubbles. Differently, a B-line was visible on both phantoms with the multi-frequency approach. Interestingly, the intensity of the B-line on phantom 1 (obtained with the bigger microbubbles) is stronger at a lower frequency, i.e. 4 MHz, than the B-line on phantom 6, which is shown on the 6 MHz image. The B-line intensity was visually assessed by the sonographer on the ultrasound videos.

It also worth noticing that on the standard US image obtained from phantom 1, A-lines are also visible at a depth of 3 cm. A-lines are horizontal artifacts caused by the reverberation of the ultrasound waves between the transducer and the lung surface (represented here by the bubble cloud positioned at a depth of 1.5 cm, and visible on the US image), and are considered to be an indication of a normal lung surface¹.

Table 1 reports the results of the visual inspection, which was performed by an experienced sonographer who was unaware of the relation between phantom type and the US video. The phantom type and the number of B-lines observed with both ultrasound imaging modalities are reported in Table 1. As regards the multi-frequency approach, the frequency at which B-lines appeared with the strongest image intensity is also indicated. Overall, considering the total number of B-lines artifacts generated by each phantom type independently on the imaging modality, B-lines appeared predominantly with phantom-type 2 (13 vs 9). Moreover, basing our findings on the multi-frequency approach, it appears that the B-lines generated with phantom-type 2 do appear at a higher frequency (4 to 6 MHz) when compared to the B-lines generated with phantom-type 1 (3 to 5 MHz).

It is also very important to observe how the appearance of B-lines strongly depends on imaging parameters. This implies that clinicians using different scanners and different probes will generally reach different conclusions, if their findings are simply based on the counting or visual characterization of the artifact.

For the authors, a deeper understanding of the artifact is key for the development of a method which can ultimately provide the clinicians with a more accurate and reliable tool.

Spectral analysis. Figure 2 shows an example of multi-frequency ultrasound images as obtained from phantom 5 (top) and 8 (bottom). A selected time window (indicated by the orange box), together with the corresponding time signals and frequency profiles, is also displayed. Moreover, color maps indicating the estimated frequency of the maximum magnitude of the power spectrum are shown, together with the corresponding color axis indicating its value in MHz.

In the absence of B-lines, the peak of the power spectra is found to be substantially identical to the center frequency of the ultrasound pulse used to generate each image, as can be seen in the color maps shown for phantom 5.

Phantom number	Phantom type	Standard US – number of B-lines	Multi-freq. US – number of B-lines	B-lines Frequency [MHz]
1	1	0	3	4
2	1	1	2	5
3	1	0	0	—
4	1	0	3	3
5	1	0	0	—
6	2	2	1	6
7	2	1	1	4
8	2	1	2	5–6
9	2	1	2	5
10	2	1	1	5–6

Table 1. Results obtained from the visual inspection of the US videos.

By contrast, in the presence of a B-line, the peak of the power spectra converges to a specific frequency, which we will refer to as the native frequency of the B-line.

This phenomenon is further illustrated in Figure 3. Here, line graphs displaying a single line of the color maps obtained from phantom 3 and 7 are shown. As can be seen in Figure 3, the maximum of the power spectrum, which is obtained for phantom 7 when the US pulse centered at 6 MHz is used, shifts towards 4.5 MHz for x ranging from 0 to 5 mm. This corresponds, in the ultrasound images, to the location of a B-line.

Discussion and Conclusion

In this paper, we have presented results from an *in-vitro* study aimed at deepening our understanding of B-line artifacts.

Two lung phantom types designed to mimic the alveolar size reduction, which is typical of several lung pathologies, were imaged using an open research platform.

These phantoms were able to generate B-line artifacts.

Standard ultrasound imaging and a multi-frequency imaging approach were used. Results show that, when standard imaging is adopted, B-lines are substantially only visible on phantom 2, which is the phantom with the smaller bubbles. This suggests a relation between bubble size (the air-space size) reduction and increased artifact formation. This observation is in line with the correlation between B-lines and a pathological condition of the lung.

When the multi frequency approach is adopted, more B-lines are visible (15 vs 7). Moreover, this imaging modality indicates that B-line formation is strongly frequency dependent, and generally dependent on the imaging modality.

Additionally, the multi-frequency approach allows us to observe that the B-lines obtained from phantom 2 are generated at higher frequencies (4 to 6 MHz) when compared to those emerging from phantom 1 (3 to 5 MHz). In particular, B-lines appeared with significantly stronger amplitude in one of the four images obtained with the multi-frequency approach, and spectral-analysis confirmed that B-lines originate from a specific portion of the US spectrum. This means, on the one hand that the native frequency of the B-lines may be used to quantitatively evaluate the state of the lung surface, while on the other it shows that there is a need for the development of an ultrasound method that is specific and dedicated to the lung if we want to achieve reproducible and reliable medical findings by means of LUS.

Another recent attempt in this direction is the work done by K.Mohanty *et al.*¹⁹. Differently than the approach we proposed, in this paper the authors investigated (*ex-vivo* and *in-vivo*) the possibility to use diffusion constant and transport mean free path estimation as a way to quantitatively characterize the micro-architecture of the lung parenchyma, and ultimately predict the extent of pulmonary edema. Their results showed how methods based on ultrasound multiple scattering could provide important information for the quantitative characterization of the lung parenchyma.

We hope that research attention in this direction will grow, and help to increase the precision and acceptance of lung ultrasonography.

To this end, our future work will focus on the validation of the results presented in this study by means of an extensive clinical study. A key aspect will be to investigate the link between the native frequency of B-lines and the condition of the lung. In parallel, new *in-vitro* study will be performed in order to assess how accurately we can relate the native frequency of the B-lines to the size and distribution of the air spaces.

Methods

Lung mimicking phantoms. Two monodisperse microbubble populations with different diameters were generated by using the MicroSphere Creator[®] (Tide Microfluidics, Enschede, the Netherlands). These micro-bubbles consisted of air-bubbles encapsulated in a lipid shell. Subsequently, ten lung-mimicking phantoms were developed. These consisted of a layer of one of the above-mentioned microbubble populations trapped in tissue-mimicking gel. The microbubbles had a diameter equal to 170 and 80 μm , and were used to develop five type 1 phantoms and five type 2 phantoms, respectively. The biggest bubble size was defined by the largest bubbles producible by the MicroSphere Creator[®]. Next, the smallest bubble size was defined in order to achieve a good separation between the two bubbles population.

Both sizes were also chosen to attain a cluster of air bubbles which were smaller in size than a normal alveolar sac, whose diameter is approximately 280 μm ²⁰.

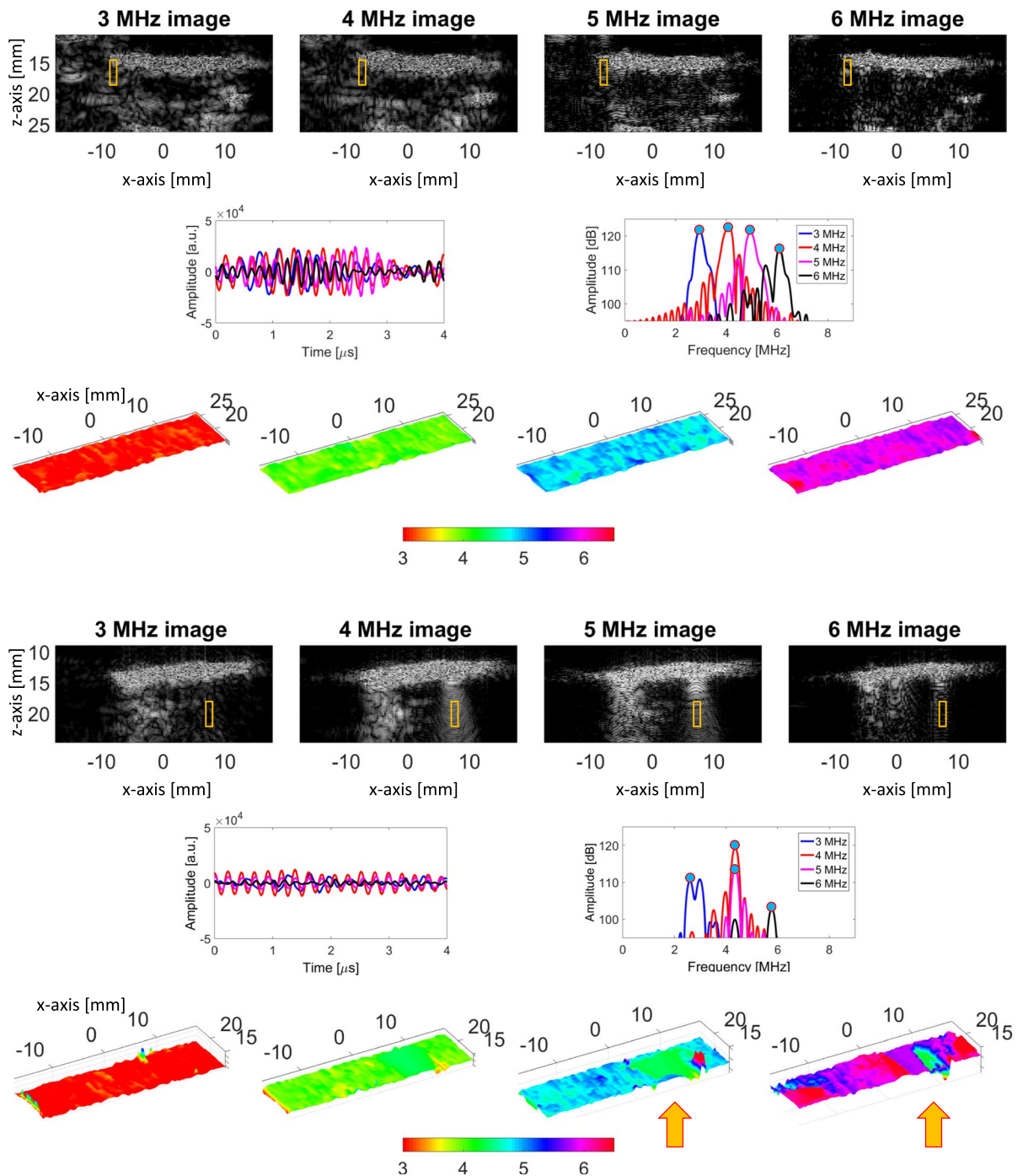


Figure 2. Ultrasound images as obtained from Phantom 5 (top) and 8 (bottom) with the multi-frequency approach are displayed, together with an example of a selected time window (orange box). The time signals and the corresponding frequency profiles are also displayed. Moreover, color maps indicating the estimated frequency of the max of the power spectrum are displayed, together with the corresponding color axis indicating its value in MHz.

Microscope images of the generated bubbles are shown in Fig. 4, together with a phantom schema and a picture of a lung mimicking phantom. The clouds of microbubbles, located at a depth of approximately 1.5 to 2.5 cm from the top of the gelatin phantom, where the US probe was positioned for imaging.

In the literature, alternative experimental models able to generate B-lines have been reported. Differently than the model presented in this study these models were based on gelatin phantoms containing large air bubbles (mm size) obtained by manual injection of air by means of a syringe²¹, sponges^{22,23} and foams²⁴.

Imaging protocol. A LA332® (Esaote, Florence, Italy) linear-array probe was connected to the ULA-OP research platform²⁵ and used for imaging. A sub-aperture consisting of 64 elements was used in transmit and receive mode, and

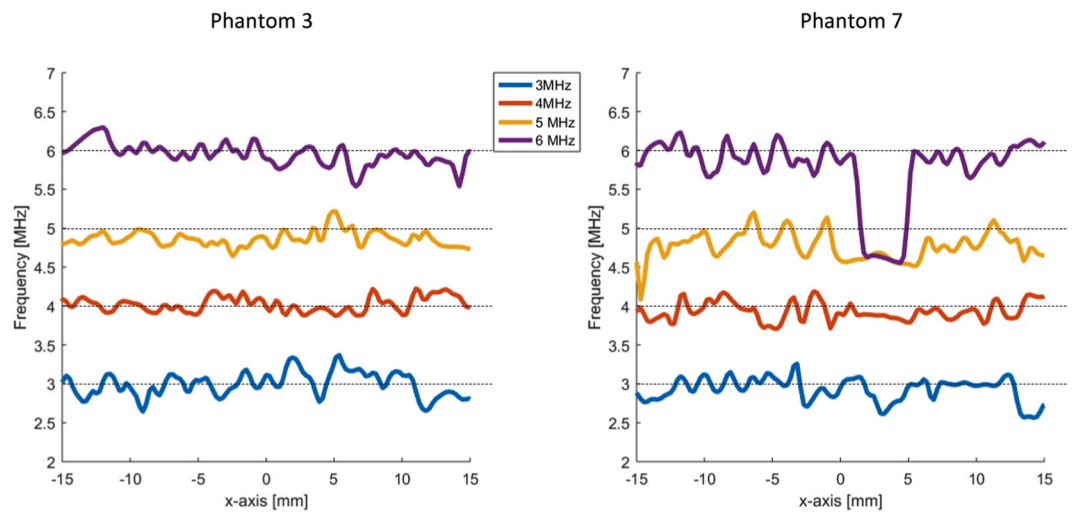


Figure 3. Line graphs displaying a single line of the color maps obtained from phantom 3 and 7.

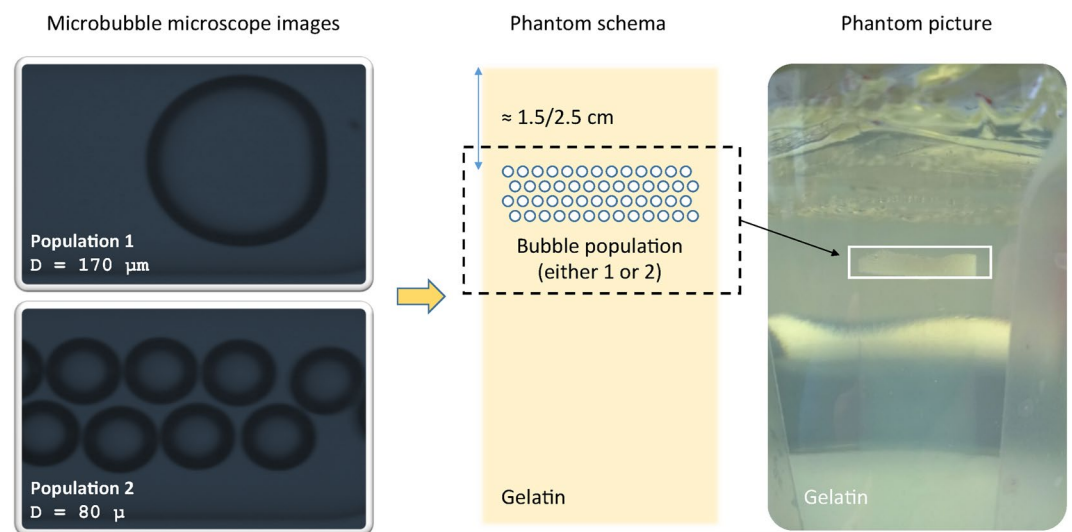


Figure 4. Microscope images of the generated microbubbles, together with a phantom schema and a picture of a lung mimicking phantom.

was linearly shifted over the array to obtain a final image consisting of 129 lines. In transmit mode, the focus was set at the depth of the microbubble cloud, and dynamic beamforming was used in receive mode. Time gain compensation parameters were set experimentally to obtain a good signal to noise ratio (and to avoid saturation) for the signals that were measured at greater depths than the bubble cloud, and were maintained unmodified for all the acquisitions.

Here, with the term “greater depths” we intend received after a longer time delay.

First, standard US imaging at 4.5 MHz was performed. In this case a 0.5- μ s Gaussian pulse was used as a driving signal.

Subsequently, a multi-frequency approach was used: images were sequentially generated using orthogonal sub-bands centered at different center frequencies, i.e., at 3, 4, 5, and 6 MHz. To keep the absolute bandwidth constant when transmitting at the different center frequencies, an absolute pulse time-length of 2 μ s was maintained for every frequency. Moreover, in this way the different pulses allowed us to cover the same bandwidth excited by the 4.5 MHz pulse, and guarantee a -10 dB orthogonality in the frequency domain. Figure 5 shows the normalized power spectra of the different driving signals. The echo signals received at the probe were digitized at a sampling frequency of 50 MHz.

For each phantom, standard US imaging at 4.5 MHz was performed first. The US probe was manually operated and translated so as to cover the entire bubble cloud. An US video was thus recorded.

Subsequently, the number of B-lines was visually assessed by an expert sonographer who was unaware of the phantom type that corresponded to each US video. The same procedure was then repeated with the multi-frequency approach, where the four images corresponding to the four different frequencies were displayed in real time. Subsequently, the probe was positioned back at the location where a B-line was observed, and raw data were recorded with the multi-frequency modality.

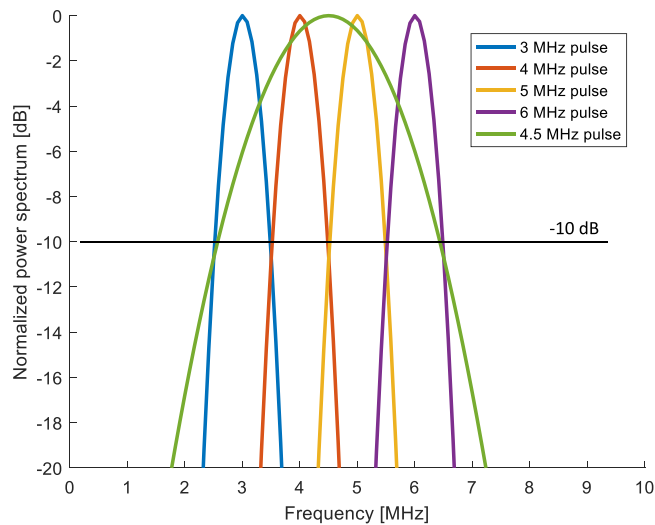


Figure 5. Normalized frequency spectra of the driving signals. The 4.5 MHz pulse was used to perform standard US imaging, while the other pulses were used for the multi-frequency approach.

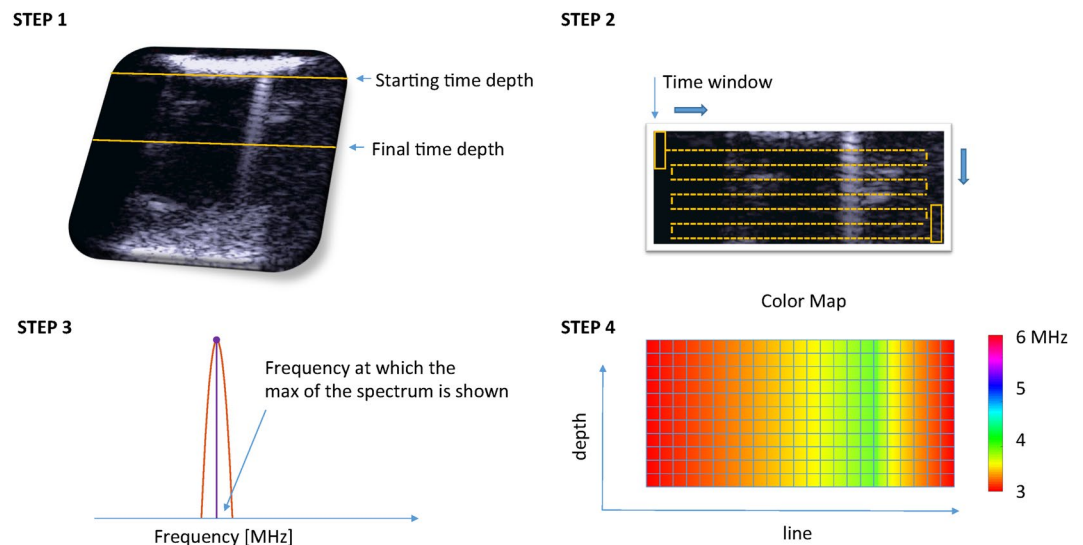


Figure 6. Schematic representation of the method that was used to process the raw data.

The data necessary to form ten image-frames were recorded for each transmitted frequency.

Raw data analysis. The US raw data were processed to analyze the spectra of the signals received from the phantoms. A four-step process was applied. In step 1, a part of the data which started from the time depth at which the first echoes (just after the bubble cloud) were received was selected. This, when compared to *in-vivo* data, is equivalent to analyzing the ultrasound echoes received after the pleura line¹. The final time depth to be selected was then obtained by considering a time depth up to a maximum of 13 μ s (approximately 1 cm) from the starting time depth. In step 2, a time window of 4 μ s was extracted from the selected data. This time window was then shifted by one line (horizontally) and by a 0.02 μ s time-step (vertically) so as to cover the entire data-set. This process resulted in 129 time signals for each of the (650) selected depths for each (10) frame of each multi-frequency approach (4) image as obtained from each (10) phantom. These signals were FFT transformed in step 3, and their power spectra analyzed. In particular, the location of the peak in the power spectra was evaluated. In step 4, a 129 (lines) by 650 (depths) by 10 (frames) matrix with values ranging from 3 to 6 MHz was obtained for each transmitted frequency. This matrix was averaged over the frames, and a color map was obtained for each image generated with the multi-frequency approach. Figure 6 visually describes the procedure. Apart from the selection of the starting time-depth, the process was automated and implemented in Matlab[®].

References

- Volpicelli, G. *et al.* International Liaison Committee on Lung Ultrasound (ILC-LUS) for the International Consensus Conference on Lung Ultrasound (ICC-LUS), International evidence-based recommendations for point-of-care lung ultrasound. *Intensive care medicine*. **38**, 577–591 (2012).
- Dunn, F. & Fry, W. J. Ultrasonic absorption and reflection by lung tissue. *Physics in Medicine and Biology*. **5**, 401–410 (1961).
- Bauld, T. J. & Schwan, H. P. Attenuation and reflection of ultrasound in canine lung tissue. *Journal of the Acoustical Society of America*. **56**, 1630–37 (1974).
- Pedersen, P. C. & Ozcan, H. S. Ultrasound properties of lung tissue and their Measurements. *Ultrasound in Medicine and Biology*. **12**, 483–99 (1986).
- Dunn, F. Attenuation and speed of ultrasound in lung: dependence upon frequency and inflation. *Journal of the Acoustical Society of America*. **80**, 1248–50 (1986).
- Dunn, F. Attenuation and speed of ultrasound in lung. *Journal of the Acoustical Society of America*. **56**, 1638–39 (1986).
- Mikhak, Z. & Pedersen, P. C. Acoustic attenuation properties of the lung: An open question. *Ultrasound in Medicine and Biology*. **28**, 1209–1216 (2002).
- Soldati, G., Demi, M., Inchingolo, R., Smargiassi, A. & Demi, L. On the Physical Basis of Pulmonary Sonographic Interstitial Syndrome. *Journal of Ultrasound in Medicine*. **35**, 2075–86 (2016).
- Jambrik, Z. *et al.* Usefulness of ultrasound lung comets as non-radiologic sign of extravascular lung water. *The American Journal of Cardiology*. **93**, 1265–1270 (2004).
- Gargani, L. *et al.* Ultrasound lung comets for differential diagnosis of acute cardiogenic dyspnea: A comparison with natriuretic peptides. *European Journal of Heart Failure*. **10**, 70–77 (2008).
- Reissig, A. & Kroegel, C. Transthoracic sonography of diffuse parenchymal lung disease. *Journal of Ultrasound in Medicine*. **22**, 173–180 (2003).
- Volpicelli, G. *et al.* Bedside lung ultrasound in the assessment of alveolar interstitial syndrome. *The American Journal of Emergency Medicine*. **24**, 689–696 (2006).
- Copetti, R., Soldati, G. & Copetti, P. Chest sonography: A useful tool to differentiate acute cardiogenic pulmonary edema from acute respiratory distress syndrome. *Cardiovascular Ultrasound*. **6**, 6–16 (2008).
- Volpicelli, G. & Frascisco, M. F. Sonographic detection of radio-occult interstitial lung involvement in measles pneumonitis. *The American Journal of Emergency Medicine*. **27**, 128.e1–128.e3 (2009).
- Soldati, G. *et al.* Ultrasonography in lung contusion. *Chest*. **130**, 533–538 (2006).
- Soldati, G. *et al.* Lung Ultrasonography may provide an indirect estimation of lung porosity and airspace geometry. *Respiration*. **88**, 548–468 (2014).
- Lichtenstein, D., Meziere, G., Biderman, P., Gepner, A. & Barre, O. The comet-tail artifact. An ultrasound sign of alveolar-interstitial syndrome. *American Journal of Respiratory and Critical Care Medicine*. **156**, 1640–6 (1997).
- Lichtenstein, D., Meziere, G. & Seiltz, J. The dynamic air bronchogram. A lung ultrasound sign of alveolar consolidation ruling out atelectasis. *Chest*. **135**, 1421–25 (2009).
- Mhanty, K., Blackwell, J., Egan, T. & Muller, M. Characterization of the Lung Parenchyma Using Ultrasound Multiple Scattering. *Ultrasound in Medicine and Biology*. **43**, 993–1003 (2017).
- Sagm, K. B., Rhyne, T. L., Myers, G. S. & Lees, R. S. Characterization of Normal and Abnormal Pulmonary Surface by Reflected Ultrasound. *Chest*. **74**, 29–33 (1978).
- Soldati, G., Copetti, R. & Sher, S. Sonographic interstitial syndrome: the sound of lung water. *Journal of Ultrasound in Medicine*. **28**, 163–174 (2009).
- Spinelli, A. *et al.* Realization of a poro-elastic ultrasound replica of pulmonary tissue. *Biomatter*. **1**, 37–42 (2012).
- Bluthgen, C., Sanabria, S., Frauenfelder, T., Klingmuller, V. & Rominger, M. Economical Sponge Phantom for Teaching, Understanding, and Researching A- and B-Line Reverberation Artifacts in Lung Ultrasound. *Journal of Ultrasound in Medicine*. **19**, 14266 (2017).
- Han, H. D. & Sanghun, L. A Low-Cost Training Phantom for Lung Ultrasonography. *Chest*. **150**, 1417–19 (2016).
- Boni, E. *et al.* A reconfigurable and programmable FPGA based system for non-standard ultrasound methods. *IEEE Transactions Ultrasonics, Ferroelectrics and Frequency Control*. **59**, 1378–1385 (2012).

Author Contributions

L. Demi conceived and designed the experiment. L. Demi conceived the data analysis algorithm and performed the data analysis. L. Demi and M. Demi conceived the lung mimicking phantoms. L. Demi and W. van Hove developed the lung phantoms. L. Demi and R.J.G. van Sloun implemented the imaging modalities and performed the image acquisition process. G. Soldati provided clinical expertise and performed the visual inspection of the ultrasound videos. All authors contributed to writing/revising the manuscript.

Additional Information

Supplementary information accompanies this paper at <https://doi.org/10.1038/s41598-017-13078-9>.

Competing Interests: The authors declare that they have no competing interests.

Publisher's note: Springer Nature remains neutral with regard to jurisdictional claims in published maps and institutional affiliations.



Open Access This article is licensed under a Creative Commons Attribution 4.0 International License, which permits use, sharing, adaptation, distribution and reproduction in any medium or format, as long as you give appropriate credit to the original author(s) and the source, provide a link to the Creative Commons license, and indicate if changes were made. The images or other third party material in this article are included in the article's Creative Commons license, unless indicated otherwise in a credit line to the material. If material is not included in the article's Creative Commons license and your intended use is not permitted by statutory regulation or exceeds the permitted use, you will need to obtain permission directly from the copyright holder. To view a copy of this license, visit <http://creativecommons.org/licenses/by/4.0/>.

© The Author(s) 2017